ChemComm

COMMUNICATION

View Article Online
View Journal | View Issue

Cite this: *Chem. Commun.*, 2023, 59, 11971

Received 22nd August 2023,
Accepted 12th September 2023

DOI: 10.1039/d3cc04023b

rsc.li/chemcomm

Nanoflower-like high-entropy Ni–Fe–Cr–Mn–Co (oxy)hydroxides for oxygen evolution†

Mingyuan Shi,[ab] Tianmi Tang,[b] Liyuan Xiao,[b] Jingyi Han,[b] Xue Bai,[b] Yuhang Sun,[ab] Siyu Chen,[b] Jingru Sun,[b] Yuanyuan Ma*[a] and Jingqi Guan *[b]

High-entropy materials (HEMs) have potential application value in electrocatalytic water splitting because of their unique alloy design concept and significant mixed entropy effect. Here, we synthesize a high-entropy Ni–Fe–Cr–Mn–Co (oxy)hydroxide on nickel foam (NF) by a solvothermal method. The flower-like structure of FeNiCrMnCoOOH/NF can provide abundant active sites, thus improving the oxygen evolution reaction (OER) activity. In 1 M KOH, the FeNiCrMnCoOOH/NF shows an ultra-low overpotential (η_{10}) of 201 mV for the OER, superior to FeNiCrMnAlOOH/NF, FeNiCrMnCuOOH/NF, FeNiCrMnMoOOH/NF, and FeNiCrMnCeOOH/NF. In addition, it exhibits a low η_{10} of 223 mV in 0.5 M NaCl + 1 M KOH and excellent stability. Electrochemical impedance spectroscopy measurements indicate that the synergistic effect between multiple metals accelerates charge transfer, while *in situ* Raman measurements reveal that NiOOH is a key active species for the OER. This work is of great significance for the construction of high-entropy (oxy)hydroxides for seawater electrolysis.

The world is moving in a low-carbon direction to solve the problems of energy shortage and environmental pollution. Hydrogen is one of the renewable energy sources used in industry and the cleanest energy in the world.[1–3] Electrolytic water for hydrogen production is a promising technology for the generation of clean fuel.[4] However, in the electrolytic water, due to the slow 4-electron transfer process in the OER, higher overpotential is required than that in the hydrogen evolution reaction (HER).[5,6] In addition, hydrogen production by water electrolysis is mainly based on ultrapure fresh water as a raw material, but its development is limited by the scarcity of global fresh water resources. As one of the most abundant resources on earth, seawater makes up 97% of the world's water.[7] Hence, the development prospect of the application of electrolytic seawater technology will become very broad.[8,9] However, the presence of Cl^- anions in seawater affects the electrolysis of seawater, which may result in electrode degradation or collapse, chloride ion corrosion and poor durability. Thus, it is crucial to develop electrocatalysts that are inexpensive, have good conductivity, and have high seawater corrosion resistance.

Transition metal-based (oxy)hydroxides have been widely studied for the OER due to their excellent activity and regulable three-dimensional electronic structures.[10–13] Usually, multimetallic (oxy)hydroxides exhibit higher OER activity than monometallic (oxy)hydroxides, mainly due to the heterostructure formed between different (oxy)hydroxides and the interaction between multiple elements that regulate the electronic structure.[14,15] Jiang *et al.* prepared NiFe LDH/FeOOH heterostructured nanosheets by electrodeposition for seawater electrolysis.[16] The electron interaction between NiFe LDH and FeOOH makes the NiFe LDH/FeOOH electrocatalyst have high electrocatalytic activity. Under a simulated seawater system, NiFe LDH/FeOOH needed an η_{100} of 286.2 mV.

HEMs have special properties due to their intrinsic effects. The uniform mixing of multiple elements leads to the increase of entropy and the decrease of the Gibbs free energy, increasing the OER stability. Lai *et al.* prepared NiCoFeMnCrP high-entropy nanoparticles by a combination of the sol–gel method and calcination treatment.[17] As expected, with the increase of the metal types, the OER activity of the phosphides was gradually enhanced, and NiCoFeMnCrP exhibited an η_{10} of 270 mV. As (oxy)hydroxides are candidates for OER electrocatalysts, and Fe, Ni, Cr, Mn, and Co are beneficial dopants, high-entropy (oxy)hydroxides will achieve a great synergy effect and have potential application value in the field of electrolytic water.

Herein, we *in situ* synthesized a nanoflower-like high-entropy FeNiCrMnCoOOH electrocatalyst on NF by a solvothermal method. In 1 M KOH, the as-synthesized FeNiCrMnCoOOH/NF exhibited high OER activity, which only needed an ultralow η_{10} of 201 mV. In 0.5 M NaCl + 1 M KOH, it showed a low η_{10} of 223 mV.

[a] *College of Chemistry and Chemical Engineering, Qiqihar University, Heilongjiang Province 161006, China. E-mail: mayuanyuan1219@126.com*
[b] *Institute of Physical Chemistry, College of Chemistry, Jilin University, Changchun 130021, PR China. E-mail: guanjq@jlu.edu.cn*

† Electronic supplementary information (ESI) available: Experimental details, XRD patterns, SEM images, HRTEM images, OER polarization curves, OER stability tests, *in situ* Raman spectroscopy, and XPS spectra. See DOI: https://doi.org/10.1039/d3cc04023b

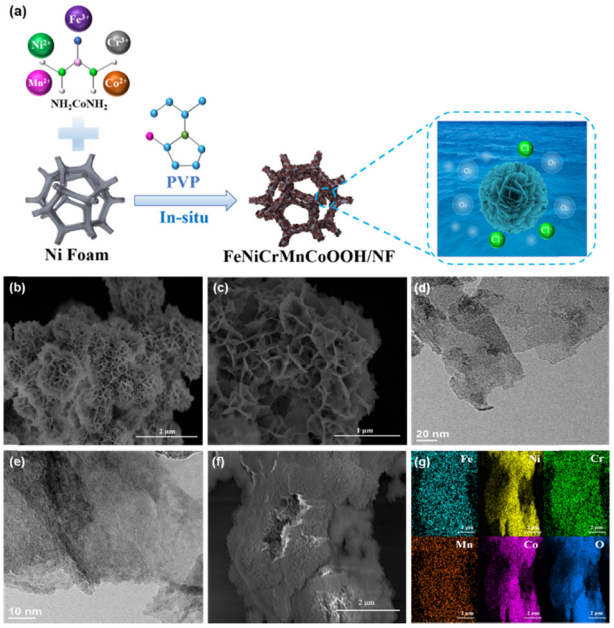

Fig. 1 (a) Schematic of the synthesis of FeNiCrMnCoOOH/NF. (b) and (c) SEM images. (d) and (e) HRTEM images. (f) SEM image, and (g) elemental mapping.

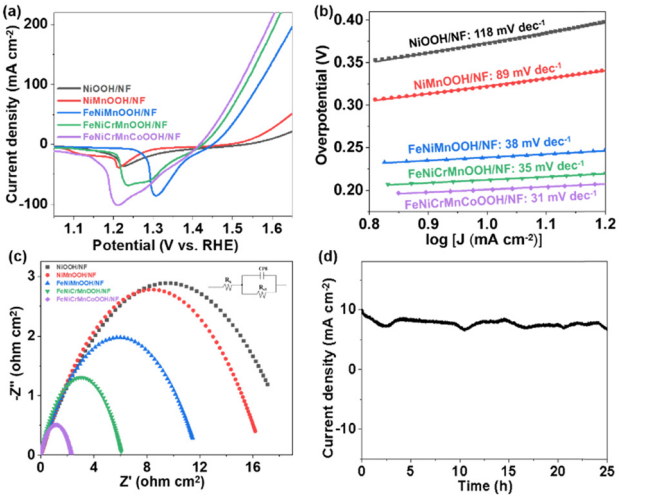

Fig. 2 (a) LSV curves of NiOOH, NiMnOOH, FeNiMnOOH, FeNiCrMnOOH and FeNiCrMnCoOOH. (b) Tafel plots. (c) EIS plots (inset: equivalent circuit model corresponding to EIS data). (d) Chronoamperometric curve of the FeNiCrMnCoOOH/NF.

In particular, because of good structural stability, it exhibited outstanding long-term stability without a significant change in current density after 25 hours of continuous operation.

A high-entropy FeNiCrMnCoOOH/NF nanoflower catalyst was synthesized by a clever and controllable solvothermal strategy using a PVP-based structure directing surfactant (Fig. 1a). The crystal structure of FeNiCrMnCoOOH/NF was analyzed by X-ray diffraction (XRD). The strong diffraction peaks at 44.7° and 51.9° are in accordance with the (111) and (200) planes of NF.[18] From the XRD results, FeNiCrMnCoOOH/NF shows amorphous properties because no significant diffraction peak due to the (oxy)hydroxides can be observed (Fig. S1, ESI†). From the SEM images, the FeNiCrMnCoOOH is uniformly decorated on the NF (Fig. S2 and S3, ESI†). As shown in Fig. 1b and c, FeNiCrMnCoOOH/NF displays a nanoflower morphology. The nanoflowers consist of ultrathin nanosheets, and the ordered array of nanosheets forms a three-dimensional structure, which can expose more active sites for adsorbing and desorbing reaction intermediates. Meanwhile, from the HRTEM images (Fig. 1d and e), no significant lattice fringe can be seen, further verifying the poor crystallinity of FeNiCrMnCoOOH/NF. The element mapping shows that Fe, Ni, Cr, Mn, Co and O elements are evenly distributed across the FeNiCrMnCoOOH/NF (Fig. 1f and g). The metal content of FeNiCrMnCoOOH/NF was analyzed by ICP-OES. As shown in Table S1 (ESI†), the molar ratio of Fe, Ni, Cr, Mn, and Co elements is approximately 1 : 1 : 1 : 1 : 1, implying that we have successfully synthesized a high-entropy FeNiCrMnCoOOH/NF electrocatalyst.

Using a common three-electrode setup, the OER performance was evaluated. As shown in Fig. 2a, FeNiCrMnCoOOH/NF shows a low η_{10} of 201 mV, much lower than NiOOH/NF (367 mV), NiMnOOH/NF (320 mV), FeNiMnOOH/NF (239 mV), FeNiCrMnOOH/NF (213 mV), and most (oxy)hydroxides reported previously (Table S2, ESI†). As depicted in Fig. S4 (ESI†), the monotonous enhancement of OER activity of the electrocatalysts from a monometallic component to a pentametallic component is observed. With the increase of the metal component, the electronic structure and the entropy can be adjusted, thereby improving the catalytic performance. Fig. 2b shows the Tafel slopes of the electrocatalysts. The Tafel slope (31 mV dec^{-1}) of FeNiCrMnCoOOH/NF is smaller than that of NiOOH/NF (118 mV dec^{-1}), NiMnOOH/NF (89 mV dec^{-1}), FeNiMnOOH/NF (38 mV dec^{-1}), and FeNiCrMnOOH/NF (35 mV dec^{-1}), demonstrating that FeNiCrMnCoOOH/NF has the fastest OER kinetic process. In addition, we have prepared a series of high-entropy (oxy)hydroxides (FeNiCrMnAlOOH/NF, FeNiCrMnCuOOH/NF, FeNiCrMnMoOOH/NF and FeNiCrMnCeOOH/NF) and evaluated their OER performance for comparison. As illustrated in Fig. S5 (ESI†), the η_{10} on the FeNiCrMnAlOOH/NF, FeNiCrMnCuOOH/NF, FeNiCrMnMoOOH/NF and FeNiCrMnCeOOH/NF is 316, 301, 280 and 266 mV, respectively, which are all higher than that on the FeNiCrMnCoOOH/NF. Meanwhile, the Tafel slopes of FeNiCrMnAlOOH/NF, FeNiCrMnCuOOH/NF, FeNiCrMnMoOOH/NF and FeNiCrMnCeOOH/NF are 126, 58, 52 and 48 mV dec^{-1}, respectively, which are larger than that of FeNiCrMnCoOOH/NF (Fig. S6, ESI†). The simultaneous introduction of Co, Fe and Ni will lead to lattice distortion and strong electronic interaction, which accelerates the adsorption of OER intermediates, thus facilitating the O_2 evolution.[19]

Electrochemical impedance spectroscopy (EIS) was used to assess the catalyst's intrinsic characteristics. As displayed in Fig. 2c, the charge transfer resistance (R_{ct}) of the FeNiCrMnCoOOH/NF is only 2.3 Ω cm^2, which is much smaller than that of NiOOH/NF (19.2 Ω cm^2), NiMnOOH/NF (16.7 Ω cm^2), FeNiMnOOH/NF (11.8 Ω cm^2) and FeNiCrMnOOH/NF (6.1 Ω cm^2), indicating that there is a strong electron interaction between

the five metals in the FeNiCrMnCoOOH/NF, improving the charge transfer ability. The OER kinetic barriers on NiOOH/NF, NiMnOOH/NF, FeNiMnOOH/NF, FeNiCrMnOOH/NF and FeNiCrMnCoOOH/NF are determined using the Arrhenius equation.[20] Compared with NiOOH/NF (25.9 kJ mol^{-1}), NiMnOOH/NF (21.8 kJ mol^{-1}), FeNiMnOOH/NF (18.7 kJ mol^{-1}) and FeNiCrMnOOH/NF (13.7 kJ mol^{-1}), the OER energy barrier of FeNiCrMnCoOOH/NF (12.4 kJ mol^{-1}) is much lower (Fig. S7 and S8, ESI†), meaning that FeNiCrMnCoOOH/NF has the lowest kinetic resistance. The excellent OER performance of FeNiCrMnCoOOH/NF was further analyzed by electrochemical active surface area (ECSA), which reflects available active sites on the catalyst surface. The ECSA of FeNiCrMnCoOOH/NF is 95 cm^2 (Fig. S9, ESI†), much higher than that of NiOOH/NF (53 cm^2) (Fig. S10, ESI†), NiMnOOH/NF (56 cm^2) (Fig. S11, ESI†), FeNiMnOOH/NF (70 cm^2) (Fig. S12, ESI†) and FeNiCrMnOOH/NF (72 cm^2) (Fig. S13, ESI†). In addition, the ECSA of FeNiCrMnAlOOH/NF, FeNiCrMnCuOOH/NF, FeNiCrMnMoOOH/NF and FeNiCrMnCeOOH/NF is 54, 80, 86 and 88 cm^2, respectively (Fig. S14–S17, ESI†). The unique flower-like structure of FeNiCrMnCoOOH/NF provides a large electrochemical active area, exposing more available active sites. The chronoamperometric curve shows that the FeNiCrMnCoOOH/NF can keep its catalytic activity during 25 h continuous testing in 1 M KOH solution (Fig. 2d), which can be attributed to the self-supporting structure, improving the binding force between the active FeNiCrMnCoOOH substance and the NF support.

Due to excellent OER performance, the FeNiCrMnCoOOH/NF was further evaluated in a simulated alkaline seawater system. As displayed in Fig. S18a (ESI†), the η_{10} on the FeNiCrMnCoOOH/NF in 0.5 M NaCl + 1 M KOH, 1 M NaCl + 1 M KOH, and 1.5 M NaCl + 1 M KOH is 223, 234 and 231 mV, respectively. At the same time, the Tafel slopes are 42, 48 and 44 mV dec^{-1}, respectively (Fig. S18b, ESI†), indicating that FeNiCrMnCoOOH/NF still has good catalytic activity in the alkaline seawater system. The R_{ct} of FeNiCrMnCoOOH/NF in 0.5 M NaCl + 1 M KOH, 1 M NaCl + 1 M KOH, and 1.5 M NaCl + 1 M KOH is 2.8, 4.7 and 3.5 Ω cm^2, respectively (Fig. S18c, ESI†), slightly higher than that in pure alkaline solution. Fig. S18d (ESI†) shows that FeNiCrMnCoOOH has excellent stability after long-term OER operation in 0.5 M NaCl + 1 M KOH electrolyte for 25 hours. In addition, the LSV curves do not change greatly before and after stability testing.

To evaluate the potential application of FeNiCrMnCoOOH/NF in electrolytic water, it was used as the anode and commercial Pt/C was used as the cathode for constructing a two-electrode system. As illustrated in Fig. S19a (ESI†), the FeNiCrMnCoOOH/NF||Pt/C electrolyzer needs a cell voltage of 1.54 V to produce a current density of 10 mA cm^{-2}, much lower than that of the IrO_2||Pt/C electrolyzer of 1.63 V. The performance of the FeNiCrMnCoOOH/NF||Pt/C electrolyzer at 10 mA cm^{-2} can be maintained for at least 25 hours without significant degradation (Fig. S19b, ESI†).

To probe the active species of FeNiCrMnCoOOH/NF for the OER, we performed *in situ* Raman characterization. As illustrated in Fig. 3a, FeNiCrMnCoOOH/NF shows two major Raman signals at 476 and 560 cm^{-1}, which can be attributed

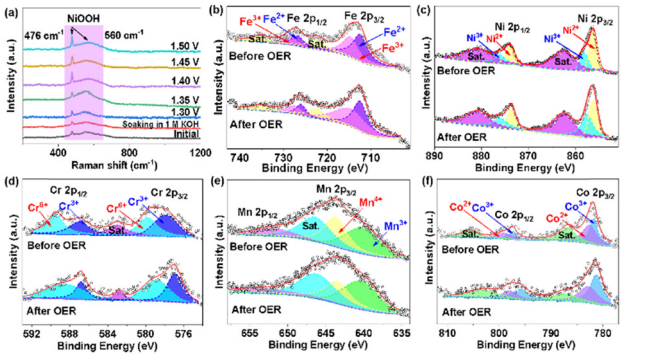

Fig. 3 (a) *In situ* Raman spectra collected on the FeNiCrMnCoOOH/NF electrode. XPS spectrum of (b) Fe 2p, (c) Ni 2p, (d) Cr 2p, (e) Mn 2p and (f) Co 2p for FeNiCrMnCoOOH/NF before and after the OER.

to the NiOOH species.[21] With increasing the applied potential, the peak intensity at 476 cm^{-1} increases significantly, indicating that the NiOOH species should be involved in the OER and is a main active species. Moreover, no signals due to other M–OOH intermediates are observed, further suggesting that the Ni site is the active site in the system. To better comprehend the elemental compositions on the catalyst surface and their valence states, the XPS spectra of the FeNiCrMnCoOOH/NF before and after OER testing were analyzed. As exhibited in Fig. S20 (ESI†), Fe, Co, Ni, Cr, Mn and O elements are detected. Fig. 3b–f exhibits the fitted XPS spectra of each element before and after the OER. The Fe 2p spectra can be split into Fe $2p_{1/2}$ (726.9 eV) and Fe $2p_{3/2}$ (712.6 eV) (Fig. 3b), characteristic of Fe^{2+},[22] and Fe $2p_{1/2}$ (728.7 eV) and Fe $2p_{3/2}$ (715 eV), attributed to Fe^{3+}. After the OER, the ratio of Fe^{2+}/Fe^{3+} becomes smaller, indicating that Fe^{2+} is partially oxidized to Fe^{3+}. The Ni 2p spectra are deconvoluted into two main contributions (Fig. 3c), corresponding to Ni^{2+} and Ni^{3+}. After the OER, the relative percentage of Ni^{3+} content significantly increases, representing that the conversion of nickel species to (oxy)hydroxides in consistent with those obtained by *in situ* Raman. Fig. 3d exhibits that the two fitting peaks at 577.9 and 587 eV correspond to Cr^{3+}, and the other fitting peaks can be ascribed to Cr^{6+}. After the OER, the percentage of Cr^{6+} significantly increases. The binding energies of Mn $2p_{3/2}$ at 640.3 eV and 643.8 eV correspond to Mn^{3+} and Mn^{4+}, respectively (Fig. 3e). After the OER, the Mn $2p_{3/2}$ peak moves to a lower binding energy, implying the increase of the Mn^{3+} content. The Co 2p XPS spectra show two double peaks related to the Co^{2+} and Co^{3+} chemical environments. After the OER, the full Co 2p XPS spectrum shifts significantly to lower binding energies (Fig. 3f) and the Co^{3+}/Co^{2+} ratio rises, indicating the formation of CoOOH species on the HEM surface.[23,24] The CoOOH generated during the OER can stabilize the OH^- on the catalyst surface, increase the conductivity and improve the charge transfer ability. The O 1s spectra show three peaks at 531.5, 532.2 and 533.9 eV, attributable to M–O, hydroxyl groups, and the adsorbed water, respectively (Fig. S21, ESI†).[25,26] The M–OH/M–O ratio increases after OER activation, revealing the formation of M–OOH in the FeNiCrMnCoOOH/NF.[27] The XPS

results indicate that after the OER, the electronic structure is adjusted due to the interaction between various elements, resulting in a shift in binding energy. After the reaction, the percentage of Fe^{3+}, Ni^{3+}, Co^{3+} and Cr^{6+} content increases significantly, and the presence of large amounts of Fe^{3+}, Ni^{3+}, Co^{3+} and Cr^{6+} has a strong oxidation capacity, which is conducive to improving the OER performance. The morphology of the catalyst after the OER was characterized by SEM. As illustrated in Fig. S22 (ESI†), the nanoflower-like morphology remains well, showing that the structure of FeNiCrMnCoOOH/NF is stable and no surface damage occurred during the OER.

In conclusion, we have successfully constructed a high-entropy nanoflower-like FeNiCrMnCoOOH/NF by a facile solvothermal method for high-efficiency OER. The FeNiCrMnCoOOH/NF showed remarkable OER activity in 1 M KOH and in 0.5 M NaCl + 1 M KOH, with an η_{10} of 201 and 223 mV, respectively, and excellent stability. The excellent OER performance can be attributed to the special flower-like structure providing more reaction sites, and the synergistic effect between the pentametallic components accelerating the charge transfer and reducing the reaction barrier, thereby improving the electrocatalytic performance. *In situ* Raman analysis reveals that NiOOH is a main active species for the OER.

This work was supported by the National Natural Science Foundation of China (No. 22075099), the Natural Science Foundation of Jilin Province (No. 20220101051JC), and the Basic Science Research Project of Heilongjiang Provincial University (No. 145109109).

Conflicts of interest

There are no conflicts to declare.

References

1 L. Yu, H. B. Wu and X. W. Lou, *Acc. Chem. Res.*, 2017, **50**, 293–301.
2 S. A. Chen, S. S. Thind and A. C. Chen, *Electrochem. Commun.*, 2016, **63**, 10–17.
3 X. L. Xiong, C. You, Z. Liu, A. M. Asiri and X. P. Sun, *ACS Sustainable Chem. Eng.*, 2018, **6**, 2883–2887.
4 J. Y. Zhang, H. M. Wang, Y. F. Tian, Y. Yan, Q. Xue, T. He, H. F. Liu, C. D. Wang, Y. Chen and B. Y. Xia, *Angew. Chem., Int. Ed.*, 2018, **57**, 7649–7653.
5 Y. Zhou, Y. S. Wu, D. X. Guo, J. L. Li, Y. Li, X. Yang, S. S. Fu, G. Z. Sui and D. F. Chai, *ACS Appl. Mater. Interface*, 2023, **15**, 15797–15809.
6 W. L. Ding, Y. H. Cao, H. Liu, A. X. Wang, C. J. Zhang and X. R. Zheng, *Rare Met.*, 2021, **40**, 1373–1382.
7 A. N. Angelakis, M. Valipour, K. H. Choo, A. T. Ahmed, A. Baba, R. Kumar, G. S. Toor and Z. W. Wang, *Water*, 2021, **13**, 2222.
8 S. Q. Jiang, H. L. Suo, T. Zhang, C. Z. Liao, Y. X. Wang, Q. L. Zhao and W. H. Lai, *Catalysts*, 2022, **12**, 123.
9 X. Bai, L. M. Wang, B. Nan, T. M. Tang, X. D. Niu and J. Q. Guan, *Nano Res.*, 2022, **15**, 6019–6025.
10 Z. L. Zhu, C. X. Xu, Y. C. Wang, L. Wang, Z. Chang, Z. W. Fang, X. T. Liu and J. G. Cheng, *J. Alloys Compd.*, 2022, **894**, 162393.
11 L. C. Bai, S. W. Lee and X. L. Hu, *Angew. Chem., Int. Ed.*, 2021, **60**, 3095–3103.
12 J. Y. Han and J. Q. Guan, *Nano Res.*, 2022, **16**, 1913–1966.
13 J. Y. Han, X. D. Niu and J. Q. Guan, *J. Colloid Interface Sci.*, 2023, **635**, 167–175.
14 J. Y. Xu, X. Zhong, X. F. Wu, Y. Wang and S. H. Feng, *J. Energy Chem.*, 2022, **71**, 129–140.
15 Z. Z. Yin, R. Z. He, Y. C. Zhang, L. G. Feng, X. Wu, T. Wagberg and G. Z. Hu, *J. Energy Chem.*, 2022, **69**, 585–592.
16 K. Jiang, W. J. Liu, W. Lai, M. L. Wang, Q. Li, Z. L. Wang, J. J. Yuan, Y. L. Deng, J. Bao and H. B. Ji, *Inorg. Chem.*, 2021, **60**, 17371–17378.
17 D. W. Lai, Q. L. Kang, F. Gao and Q. Y. Lu, *J. Mater. Chem. A*, 2021, **9**, 17913–17922.
18 H. X. Liao, T. Luo, P. F. Tan, K. J. Chen, L. L. Lu, Y. Liu, M. Liu and J. Pan, *Adv. Funct. Mater.*, 2021, **31**, 2102772.
19 X. W. Pang, H. T. Geng, S. W. Dong, B. G. An, S. M. Zheng and B. Wang, *Small*, 2023, **19**, 2205525.
20 J. R. Swierk, S. Klaus, L. Trotochaud, A. T. Bell and T. D. Tilley, *J. Phys. Chem. C*, 2015, **119**, 19022–19029.
21 X. H. Liu and J. Wu, *Electrochim. Acta*, 2019, **320**, 134577.
22 M. Zhu, B. Z. Zhao, Y. F. Yuan, S. Y. Guo and G. Y. Wei, *J. Electroanal. Chem.*, 2021, **882**, 115026.
23 C. Wang, P. L. Zhai, M. Y. Xia, Y. Z. Wu, B. Zhang, Z. W. Li, L. Ran, J. F. Gao, X. M. Zhang, Z. Z. Fan, L. C. Sun and J. G. Hou, *Angew. Chem., Int. Ed.*, 2021, **60**, 27126–27134.
24 A. Saad, Y. Gao, A. Ramiere, T. Z. Chu, G. Yasin, Y. Y. Wu, S. Ibraheem, M. Wang, H. C. Guo, P. Tsiakaras and X. K. Cai, *Small*, 2022, **18**, 2201067.
25 T. T. Zhou, Z. Cao, P. Zhang, H. Y. Ma, Z. Gao, H. Wang, Y. Lu, J. He and Y. F. Zhao, *Sci. Rep.*, 2017, **7**, 46154.
26 X. Chen, Z. J. Qiu, H. L. Xing, S. X. Fei, J. Z. Li, L. B. Ma, Y. T. Li and D. M. Liu, *Appl. Catal., B*, 2022, **305**, 121030.
27 R. Liu, Y. Y. Wang, D. D. Liu, Y. Q. Zou and S. Y. Wang, *Adv. Mater.*, 2017, **29**, 1701546.

